Journal of Applied Fluid Mechanics, Vol. 8, No. 3, pp. 439- 452, 2015.
Available online at www.jafmonline.net, ISSN 1735-3572, EISSN 1735-3645.
DOI: 10.18869/acadpub.jafm.67.222.22848

A Ghost Fluid Approach for Thermal Lattice Boltzmann Method in Dealing with Heat Flux Boundary Condition in Thermal Problems with Complex Geometries

R. Khazaeli, M. Ashrafizaadeh and S. Mortazavi†

Department of Mechanical Engineering, Isfahan University of Technology, Isfahan, 84156-83111, Iran

†*Corresponding author E-mail: saeedm@cc.iut.ac.ir*

(Received March 21, 2014; accepted June 26, 2014)

ABSTRACT

In this paper, the ghost fluid thermal lattice Boltzmann method is improved to properly impose the heat flux boundary condition on complex geometries [Khazaeli, R., S. Mortazavi and M. Ashrafizaadeh (2013). Application of a ghost fluid approach for a thermal lattice Boltzmann method, J. Comput. Phys. 250, 126–140]. A double-population thermal lattice Boltzmann method is used to handle both the flow and temperature fields on a Cartesian grid and the boundary conditions are imposed using a ghost fluid method. The method is based on the decomposition of the unknown distribution functions into their equilibrium and non-equilibrium parts at every ghost point. The equilibrium parts are determined by performing an extrapolation of major quantities from the image points to the associated ghost points. The bounce-back scheme is then used to determine the non- equilibrium parts. The method benefits from some features such as easy implementation and second order accuracy. The method is applied to simulate natural convection within annuluses with different shapes and boundary conditions,. The obtained results are generally in a good agreement with those predicted by other numerical efforts.

Keywords: Ghost fluid approach; Thermal lattice Boltzmann method; Fluid flow; Heat transfer; Heat flux boundary condition; Complex geometry.

1. INTRODUCTION

In recent years, the lattice Boltzmann method (LBM) (Qian, d'Humières and Lallemand 1992; Chen and Doolen 1998) has been applied successfully as a practical alternative to traditional computational fluid dynamics (CFD). The LBM is a mesoscopic particle based approach, which solves the discrete Boltzmann equation to represent characteristics of flow by tracking evolution of a single particle distribution. The LBM is straightforward to apply, computationally efficient, numerically stable, highly accurate and easy for parallelization.

So far, several approaches have been presented to impose hydrodynamic boundary conditions for the LBM. The bounce-back approach (Cornubert, d'Humières and Levermore 1991), half-way bounce-back approach (Ziegler 1993), hydrodynamic method (Noble, Chen, Georgiadis and Buckius 1995), non-equilibrium bounce-back method (Zu and He 1997), and the extrapolation scheme (Chen, Martínez and Mei 1996) can be considered as the more popular methods.

Several thermal lattice Boltzmann methods (TLBM) have been presented to adequately simulate heat transfer phenomena. In general, current TLBM can be classified into three categories: the multispeed model (McNamara and Alder 1993; Alexander, Chen and Sterling 1993; Chen, Ohashi and Akiyama 1994), the passive scalar model (Bartoloni, Battista and Cabasino 1993; Shan 1997) and the most popular method say double population model. The double population approach proposed by He *et al*. (1998) contains an independent internal energy distribution population which enhances the numerical stability. Furthermore, the viscous dissipation term and the compression work done by pressure are included in this model. However, it is not easy to apply this method since a complicated gradient operator is included. As a result, various simplified models have been introduced in which the effects of viscous dissipation and/or pressure work in the energy equation have been neglected (Peng, Shu and Chew 2003; Shi, Zhao and Guo 2004; Li, He, Wang and Tang 2008). To construct proper thermal boundary conditions for the TLBE, so far several treatments have been presented (Tang, Tao and He 2005; D'Orazio, Corcione and Celata 2004; Liu, Lin, Mai and Lin 2010).

However, due to some limitations in the standard LBM (e.g. the requirement of using uniform orthogonal lattices and a constant time step), it is not so easy to implement boundary conditions for complex geometries. Several researches have been made (Kao and Yang 2008) to overcome such difficulties. The work of Fillipova and Hänel (1998) can be considered as the first attempt in this respect. They developed a method founded on the bounce-back rule to impose a no-slip boundary condition on the curved boundary. Later, Mei *et al*. (1999) improved this method. Guo *et al*. (2002) introduced a non-equilibrium distribution extrapolation method. A boundary condition for LBM was proposed by Chang *et al*. (2009) to simulate flows with complex geometries. Based on a reformation of the populations from the density, velocity and the strain rate, Verschaeve and Müller (2010) proposed a no-slip curved boundary treatment for the LBM. Yin and Zhang (2012) developed a novel bounce-back boundary approach for moving walls. They used a midpoint velocity interpolated/extrapolated from the boundary, and related fluid points velocities instead of the real boundary velocity to obtain the unknown populations.

On the other hand, several studies have utilized the immersed boundary method (IBM) (Peskin 1972) as another proper technique to treat fluid flows within complex geometries via the LBM (Feng and Michaelides 2004; Niu, Shu, Chew and Peng 2006; Wu and Shu 2009). In this approach, the effect of the body's wall on the fluid field is enforced by estimating a local force term.

As another flexible approach to use the ghost fluid method (GFM), Tiwari and Vanka (2012) simulated the fluid flow within complex geometries. In this method, after decomposing the density distribution function into equilibrium and non- equilibrium parts, the unknown values at each ghost point (e.g. density, velocity, and non- equilibrium parts) are estimated using an extrapolation from the image nodes within the fluid field.

In general, the GFM was proposed by Fedkiw *et al*. (1999) in dealing with the multi-medium flows. The major appealing characteristics of the GFM are its easy implementation and extension to multi-dimensions, and its preservation of a sharp interface without smearing. Recently, several researches have been conducted to develop an appropriate GFM in dealing with the fluid flow and/or heat transfer phenomenon within complex geometries. Using the GFM, Mittal *et al*. (2007) proposed a versatile sharp interface technique to treat the fluid flow with complex three-dimensional bluff bodies. Pan (2010) developed a GFM to handle both the fluid flow and heat transfer phenomenon over the immersed bodies with complex shapes. Chaudhuri *et al*. (2011) implemented the GFM in order to investigate the complex shock-obstacle interactions.

To the best of the author's knowledge, there are only a few proposed models in the open literature to treat both fluid flow and heat transfer phenomenon using the lattice Boltzmann model on complex geometries. As the first study in this respect, Huang *et al*. (2006) presented a curved boundary condition for TLBE, which is based on the idea of Guo *et al*. (2002). Here, the unknown distribution functions associated with each wall point are decomposed into their equilibrium and non- equilibrium parts. The equilibrium part is estimated using the values pertained to the boundary condition, while a first order extrapolation from the fluid points is used to determine the non- equilibrium part. Their results show a second order accuracy for the method. Using feedback forcing scheme, Jeong *et al*. (2010) imposed the curved boundary condition for both momentum and energy fields to simulate thermal flows around bluff bodies. However, this method suffers from shortcomings such as instability and arbitrariness in choosing the associated parameters (He, Chen and Doolen 1998; Kang and Hassan 2011). Moreover, using the complex double-population model (He, Chen and Doolen 1998), the implementation of this method is more complicated. Afterwards, Kang and Hassan (2011) utilized the IBM in dealing with complex thermal flows. They extended their sharp interface scheme (Kang and Hassan 2010), which is based on a second-order bilinear and a linear interpolation, into two thermal LB models: a double-population model with a simplified TLBE and a hybrid model with an advection-diffusion equation for the temperature field. A boundary condition for the TLBE was developed by Lin *et al*. (2012) to simulate natural convection with complex solid objects.

However, there is a unique work on the application of the LBM for thermal flow problems with curved Neumann (heat flux) boundary condition. Recently, Li *et al*. (2013) proposed a thermal boundary condition for the TLBE based on the bounce-back approach and interpolation of the distribution functions for both the Dirichlet and Neumann conditions. For a curved boundary, they achieved a second order accuracy in space for the Dirichlet boundary condition while for the Neumann one only a first order accuracy was achieved.

In this paper, some enhancement of the previous work of the authors (Khazaeli, Mortazavi and Ashrafizaadeh 2013) is provided to simulate the thermal problems with Neumann boundary condition on curved boundaries using the LBM. This approach is basically founded on interpolation-extrapolation methodology by applying ghost fluid method without utilizing the forcing concept (unlike Immersed boundary method). The method is general and second-order accurate. The paper is organized as follows: Section 2 introduces the ghost fluid thermal lattice Boltzmann method. In Section 2.1, the double population TLBM is described. Section 2.2 addresses the ghost fluid approach to handle complex geometries. The combination of the ghost fluid method with the LBM and also the presented hydrodynamic and thermal boundary conditions are discussed in Section 2.3. In Section 3, various heat transfer problems are simulated to validate the method and the obtained results are compared with other numerical approaches. Ultimately, a concise conclusion is drawn in Section 4.

2. THERMAL GHOST FLUID LATTICE BOLTZMANN METHOD

2.1. Thermal Lattice Boltzmann Method

In this study, we used the double population TLBM that includes two evolution equations for density distribution function, f_α, and internal energy distribution function, g_α, in order to solve the flow and temperature fields, respectively. The following equations express the approach (Khazaeli, Mortazavi and Ashrafizaadeh 2013).

$$f_i\left(\mathbf{x}+\mathbf{e}_i\Delta t, t+\Delta t\right)-f_i\left(\mathbf{x},t\right)= -\frac{1}{\tau_f}\left[f_i\left(\mathbf{x},t\right)-f_i^{eq}\left(\mathbf{x},t\right)\right]+\left(1-\frac{1}{2\tau_f}\right)F_i\,\Delta t \tag{1}$$

$$g_i\left(\mathbf{x}+\mathbf{e}_i\Delta t, t+\Delta t\right)-g_i\left(\mathbf{x},t\right)= -\frac{1}{\tau_g}\left[g_i\left(\mathbf{x},t\right)-g_i^{eq}\left(\mathbf{x},t\right)\right]+\left(1-\frac{1}{2\tau_g}\right)Q_i\,\Delta t \tag{2}$$

where $\mathbf{x}$ denotes the spatial coordinate, t and Δt show time and its interval, respectively, e_i is the lattice velocity in i^{th} lattice direction, and the relaxation times for the density and the internal energy functions are shown by τ_f and τ_g, respectively. In addition, the discrete forcing term, F_i, and energy source, Q_i, can be expressed as follow:

$$F_i\left(\mathbf{x},t\right)=w_i\left[3\frac{\mathbf{e}_i-\mathbf{u}\left(\mathbf{x},t\right)}{c^2}+9\frac{\mathbf{e}_i.\mathbf{u}\left(\mathbf{x},t\right)}{c^4}\mathbf{e}_i\right].\mathbf{F}\left(\mathbf{x},t\right) \tag{3}$$

$$Q_i\left(\mathbf{x},t\right)=w_i\,Q\left(\mathbf{x},t\right) \tag{4}$$

In the above relations, $\mathbf{F}$ and Q are the forcing term and energy source densities, respectively.

The D2Q9 model (Fig. 1) which is the two-dimensional nine-velocity LBE model on a square lattice is employed here. The density and internal energy equilibrium distribution functions in Eqs. (1) and (2) can be calculated by:

$$f_i^{eq}=w_i\rho\left[1+\frac{3}{c^2}\left(\mathbf{e}_i\cdot\mathbf{u}\right)+\frac{4.5}{c^4}\left(\mathbf{e}_i\cdot\mathbf{u}\right)^2-\frac{1.5}{c^2}\mathbf{u}^2\right],\quad i=0-8 \tag{5}$$

$$g_i^{eq}=\begin{cases} w_i\rho\varepsilon\left(\dfrac{u^2}{c^2}\right) & i=0\\ w_i\rho\varepsilon\left(1.5+1.5\dfrac{\left(\mathbf{e}_i\cdot\mathbf{u}\right)}{c^2}+4.5\dfrac{\left(\mathbf{e}_i\cdot\mathbf{u}\right)^2}{c^4}-1.5\dfrac{\mathbf{u}^2}{c^2}\right) & i=1,2,3,4\\ w_i\rho\varepsilon\left(3+6\dfrac{\left(\mathbf{e}_i\cdot\mathbf{u}\right)}{c^2}+4.5\dfrac{\left(\mathbf{e}_i\cdot\mathbf{u}\right)^2}{c^4}-1.5\dfrac{\mathbf{u}^2}{c^2}\right) & i=5,6,7,8\end{cases} \tag{6}$$

and $\mathbf{e}_i$, the discrete velocity vector is expressed as:

$$e=\begin{cases}(0,0)\\ (\cos[(i-1)\pi/2]\,,sin[(i-1)\pi/2])c\\ cos[(2i-9)\,\pi/4]\;\;,\sin[(2i-9)\,\pi/4])\sqrt{2c}\end{cases}$$

for

$$i=\begin{cases}0\\ 1,2,3,4\\ 5,6.7.8\end{cases} \tag{7}$$

where $c=\sqrt{3RT_0}$ denotes lattice speed. R and T_0 are the gas constant and the reference temperature, respectively.

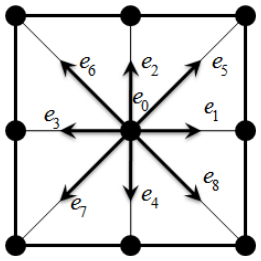

Fig. 1. Lattice links for the D2Q9 lattice Boltzmann model.

The internal energy is defined as $\varepsilon = DRT/2$, where dimension of simulation is denoted by D. Here, we considered only two-dimensional problems and consequently we set $D=2$. The weighting coefficient for the D2Q9 model is defined as:

$$w_i=\begin{cases}4/9 & i=0\\ 1/9 & i=1,2,3,4\\ 1/36 & i=5,6,7,8\end{cases} \tag{8}$$

The solution of Eqs. (1) and (2) is composed of two main computational steps known as the collision and the streaming steps and an intermediate additional step, which is the force/source adding step. Hence, these equations may be restated as:

collision step:

$$\begin{cases} f_i'\left(\mathbf{x},t\right)=f_i\left(\mathbf{x},t\right)-\dfrac{1}{\tau_f}\left[f_i\left(\mathbf{x},t\right)-f_i^{eq}\left(\mathbf{x},t\right)\right]\\ g_i'\left(\mathbf{x},t\right)=g_i\left(\mathbf{x},t\right)-\dfrac{1}{\tau_g}\left[g_i\left(\mathbf{x},t\right)-g_i^{eq}\left(\mathbf{x},t\right)\right]\end{cases} \tag{9}$$

force/source adding step:

$$\begin{cases} f_i''\left(\mathbf{x},t\right)=f_i'\left(\mathbf{x},t\right)+\left(1-\dfrac{1}{2\tau}\right)F_i\,\Delta t\\ g_i''\left(\mathbf{x},t\right)=g_i'\left(\mathbf{x},t\right)+\left(1-\dfrac{1}{2\tau_g}\right)Q_i\,\Delta t\end{cases} \tag{10}$$

streaming step:

$$\begin{cases} f_i\left(\mathbf{x}+\mathbf{e}_i\Delta t, t+\Delta t\right)=f_i''\left(\mathbf{x},t\right)\\ g_i\left(\mathbf{x}+\mathbf{e}_i\Delta t, t+\Delta t\right)=g_i''\left(\mathbf{x},t\right)\end{cases} \tag{11}$$

The direction-specific distribution functions are relaxed towards their quasi-equilibrium distributions during the collision process, and the lattice particles exchange momentum and energy in the meantime, and simultaneously the mass, momentum and energy conversation laws are satisfied over each node. Then, after experiencing the effect of the external force and energy source terms through the intermediate step, each particle goes along its related lattice links, and moves toward the adjacent points during the streaming process.

Macroscopic quantities such as the density ρ, fluid velocity $\mathbf{u}$, and the internal energy ε can then be calculated through:

$$\rho = \sum_i f_i \tag{12}$$

$$\rho \mathbf{u} = \sum_i \mathbf{e}_i f_i + \frac{\Delta t}{2}\mathbf{F} \tag{13}$$

$$\rho \varepsilon = \sum_i g_i + \frac{\Delta t}{2} Q \tag{14}$$

Also, the pressure is given by:

$$P = \frac{1}{3}\rho c^2 \tag{15}$$

It is shown that the Chapman-Enskog multi-scale analysis correctly recovers the following macroscopic continuity, momentum and energy equations

$$\begin{aligned} &\frac{\partial \rho}{\partial t} + \nabla.\rho\mathbf{u} = 0 \\ &\frac{\partial}{\partial t}(\rho\mathbf{u}) + \nabla.(\rho\mathbf{u}\mathbf{u}) = -\nabla P \\ &+\upsilon\nabla.\left[\rho\nabla\mathbf{u} + (\rho\nabla\mathbf{u})^T\right] + F \\ &\frac{\partial}{\partial t}(\rho\varepsilon) + \nabla.(\rho\varepsilon\mathbf{u}) = \alpha\nabla^2(\rho\varepsilon) + Q \end{aligned} \tag{16}$$

where the kinematic viscosity, υ, and thermal diffusivity, α, are represented as:

$$\begin{aligned} \upsilon &= \frac{1}{3}\left(\tau_f - \frac{1}{2}\right)c^2\Delta t \\ \alpha &= \frac{2}{3}\left(\tau_g - \frac{1}{2}\right)c^2\Delta t \end{aligned} \tag{17}$$

It is necessary to state that throughout this study, the time increment and lattice space are $\Delta t = \Delta x = 1$, and we have set $c = 1$. Moreover, no energy source is considered in the simulations and hence, the last term in the right-hand side of Eq. (2) simply vanishes.

2.2 Ghost Fluid Approach

In the present study, ghost fluid thermal lattice Boltzmann method (GFTLBM) applied in (Khazaeli, Mortazavi and Ashrafizaadeh 2013) has been adopted.

Fig. 2 illustrates a schematic diagram of the ghost points arrangement, where the computational domain is divided into two separate regions: a physical domain, Ω_p, and a solid domain Ω_s. The fluid pointes (*FPs*) are placed within the physical domain while the ghost points (*GPs*) are located inside the body points (*BPs*) adjacent to the fluid-solid demarcation. The practical ghost-fluid approach consists of two major steps. First, a list of ghost points in the whole domain is determined. This list includes every point inside the solid domain which has at least one neighbor point inside the fluid domain. The second step is to obtain all variables needed to form the distribution function for all ghost points belonging to the list.

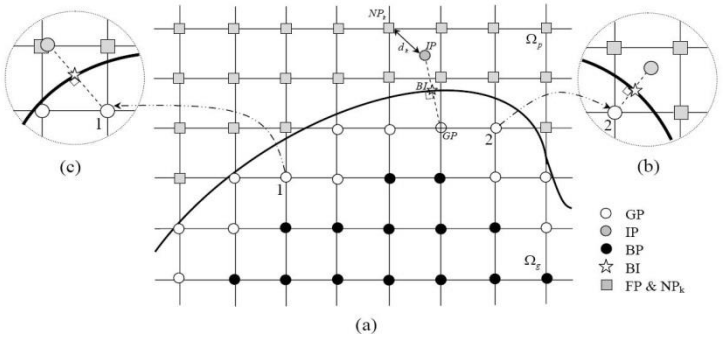

Fig. 2. Schematic illustration of the immersed boundary treatment: (a) regular ghost point arrangement with for neighboring fluid points; (b) special case of one neighboring point belonging to solid domain; (c) special case of image point very close to one neighboring point.

The procedure is as follows:

1. For each ghost point (*GP*) an image point (*IP*) should be determined. For this purpose, from each *GP* , the boundary intercept (*BI*) is defined by extending a line segment perpendicular to the nearest boundary segment.Then, the image point (*IP*) is obtained inside the fluid domain by mirroring the line with respect to the boundary profile (by stretching the line into the fluid domain such that the boundary intercept is halfway between the ghost point and the image point) (Fig. 2a).

2. The main flow variables at *IPs* are then interpolated. There are several interpolation methods. In our previous study (Khazaeli, Mortazavi and Ashrafizaadeh 2013), the inverse distance weighting interpolation was used. However, here, we used another interpolation scheme which is more accurate. Following the study of Mittal *et al.* (2008), a bilinear interpolation with the following form is utilized to estimate the value of a general variable say Γ_{IP} from four nods surrounding the *IP* (NP_k with $k=1...4$):

$$\Gamma_{IP} = C_1 xy + C_2 x + C_3 y + C_4 \tag{18}$$

where, x and y are the Cartesian coordinate of the image point. The four unknown coefficients are determined in terms of the variable values of the four surrounding points:

$$\{C\} = \left[V\right]^{-1} \{\Gamma\} \tag{19}$$

where $\{C\}^T$ is the vector including the four unknown coefficients, and $\left[\Gamma\right]^T$ is the vector containing the variable values at the four surrounding points. Besides, [V] is the Vandermonde matrix related to the bilinear interpolation method explained in Eq. (15) and has the following form:

$$[V] = \begin{bmatrix} x_1 y_1 & x_1 & y_1 & 1 \\ x_2 y_2 & x_2 & y_2 & 1 \\ x_3 y_3 & x_3 & y_3 & 1 \\ x_4 y_4 & x_4 & y_4 & 1 \end{bmatrix} \tag{17}$$

In the above procedure, there are some cases which need particular consideration, containing cases with $NP_k \in \Omega_g$ (Fig. 2b). For the former case, following the work of Tiwari and Vanka (2012), these points can be replaced by the corresponding boundary intercept points. However, using this method, it was seen that the result for the cases with heat flux on the curved boundary are not reasonable. Besides, using the interpolation used in our previous work (Khazaeli, Mortazavi and Ashrafizaadeh 2013) some oscillations near the curved boundary appear for the cases with heat flux boundary condition. Perhaps this is due to the fact that the value of image points is obtained by three or even two points for the former case. This can lead to a decrease in the accuracy of estimating the values at ghost points. Consequently, we prefer to utilize the method used by Mittal *et al.* (2008) (to solve a coupled system). However, since problems considered here are all steady state, we used the variable values of ghost fluid obtained in the last time step. Another point here is that we located the outer planar boundaries at half-way between two grid lines, for convenience. This strategy causes the *IPs* to be coinciding with the first grid nodes next to the outer boundaries**.** Therefore**,** there is no need to perform interpolation for estimating the main flow variables at *IPs*. For a corner *GP*, our treatment is to average over the major quantities at the two adjoining *GPs* (see step 3 in the following) and associate the values to such *GP*.

3. Finally, to appropriately enforce the hydrodynamic or thermal boundary conditions for the fluid-solid interface, the main flow variables at each *IP* should be extrapolated to the related *GP*. For a Dirichlet boundary condition, the following straightforward second order relation is used to extrapolate the variables:

$$\Gamma_{GP} = 2\Gamma_{BI} - \Gamma_{IP} \tag{20}$$

Furthermore, the following second-order central-difference scheme is used to employ the Neumann boundary condition:

$$\left(\frac{\partial \Gamma}{\partial n}\right)_{BP} = \frac{\Gamma_{IP} - \Gamma_{GP}}{\Delta \ell} + \mathbf{O}\left(\Delta \ell^2\right) \tag{21}$$

Wwhere, $\left(\partial\Gamma/\partial n\right)$ is the gradient of the major quantities at the boundary along the perpendicular direction, $\mathbf{n}$ denotes local unit outward normal to the boundary profile, and $\Delta\ell$ represents the spatial distance between the GP and the IP. Therefore, we impose the heat flux on BIs by calculating the quantities at the *GPs* as follows:

$$\Gamma_{GP} = \Gamma_{IP} - \Delta \ell \left(\frac{\delta \Gamma}{\delta n}\right)_{BP} \tag{22}$$

For the density at the *GPs*, however, we have:

$$\rho_{GP} = \rho_{IP} \tag{23}$$

2.3. Combination the Thermal Lattice Boltzmann Method and the Ghost Fluid Approach

To accurately satisfy boundary conditions in LBM, specifying the unknown values at the points belonging to the solid domain and adjacent to the interface is a critical step. The final step is to compute the density and energy distribution functions at each *GP* by means of the data obtained via the interpolation (as mentioned in the previous Subsection). To perform this, we adopted the non-equilibrium bounce-back method (Peng, Shu and Chew 2003) as the boundary condition for both flow and thermal boundary conditions. In this approach we decompose the unknown distribution functions into equilibrium and non-equilibrium parts. The equilibrium parts are then estimated by Eqs. (5) and (6) through the values obtained by interpolation. However, the non-equilibrium parts are evaluated by applying the non-equilibrium bounce-back method as follows:

$$\begin{aligned} & f_i^{neq}\left(GP,t\right) = f_{\bar{i}}^{neq}\left(IP,t\right) \\ & g_i^{neq}\left(GP,t\right) = -g_{\bar{i}}^{neq}\left(IP,t\right) \\ & +(\mathbf{e}_i^2 + \mathbf{e}_{\bar{i}}^2) \times f_{\bar{i}}^{neq}\left(IP,t\right) \end{aligned} \tag{24}$$

Where $f^{neq} = f - f^{eq}$, $g^{neq} = g - g^{eq}$, and $\mathbf{e}_{\bar{i}} = -\mathbf{e}_i$. Here $f^{neq}(IP)$ and $g^{neq}(IP)$ are calculated in the same way as for the Γ_{IP}. In other words the non-equilibrium distribution functions at any IP are interpolated using those at the neighbor points via the interpolation scheme described above. We note that in our previous work (Khazaeli, Mortazavi and Ashrafizaadeh 2013) we eliminated the second part in the right hand side of the second equation in Eq. 21. But, here, it was found that it is necessary to use the whole relation proposed by He *et al*. (1998) in order to reach more accurate results. Ultimately, the equilibrium and non-equilibrium parts at each *GP* are added together to determine the density and energy distribution functions:

$$\begin{aligned} f_i(GP,t) &= f_i^{eq}(GP,t) + f_i^{neq}(GP,t) \\ g_i(GP,t) &= g_i^{eq}(GP,t) + g_i^{neq}(GP,t) \end{aligned} \tag{25}$$

3. RESULTS AND DISCUSSION

3.1. Natural Convection in a Horizontal Enclosure with an Adiabatic Circular Cylinder

In order to reveal the capability of the proposed approach, the natural convection of a fluid in an annulus at different Rayleigh numbers has been considered. As can be seen from Fig. 3(a), the geometry consists of a two-dimensional rectangular enclosure with length L and a circular cylinder of radius r_c which are concentrically placed. The left wall of cavity is maintained at the high temperature T_h whereas the right one is kept at the low temperature T_c. Moreover, the top and bottom walls of cavity and also the cylinder wall were assumed adiabatic. Note here that, both cavity and circular cylinder walls are considered to be stationary.

The aspect ratio between the enclosure and the circular cylinder is defined as $\lambda = L/2r_c$ and is set to $\lambda = 2.5$. Here, we assumed the fluid properties to be constant, aside from the density in the buoyancy term, which adopts the Boussinesq approximation. The external force term $\mathbf{F}$ in Eq. (3), corresponds to the buoyancy force, and is evaluated by $\mathbf{F} = -\rho\beta(T - T_c)\mathbf{g}$, where $\mathbf{g}$ represents the gravitational acceleration vector acting in the negative vertical direction, and β is the thermal expansion coefficient at T_C. The Rayleigh number, Ra, and the Prandtl number, Pr, are the main control parameters for this problem and are defined as:

$$Ra = \frac{g\beta(T_H - T_C)L^3}{\nu\alpha} \quad , \quad \Pr = \frac{\upsilon}{\alpha} \tag{26}$$

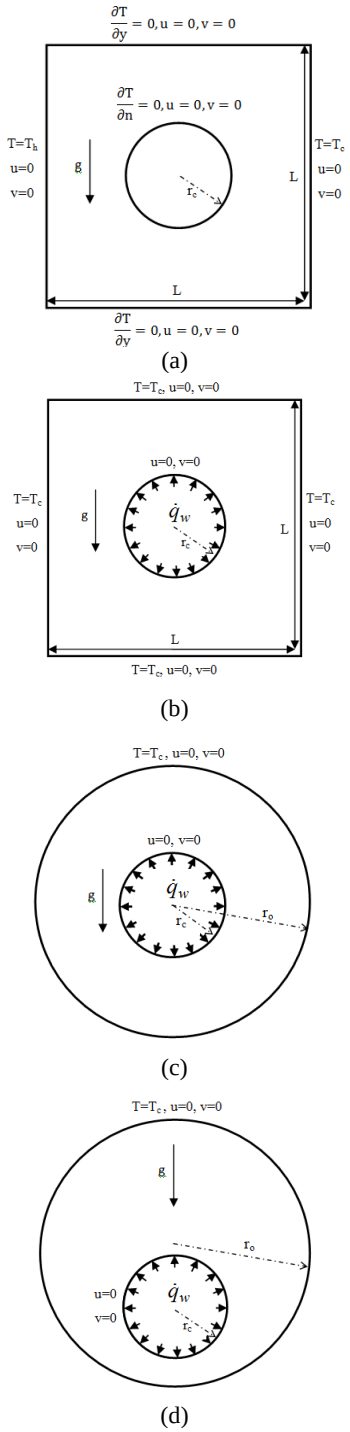

Fig. 3. Schematic of configuration and boundary conditions pertained to the problems under consideration.

Defining the characteristic velocity as $U_c = \sqrt{\beta g \Delta T L}$, the viscosity, thermal diffusivity, and the relaxation times can be rewritten in the following forms:

$$\begin{aligned} \nu &= \sqrt{\frac{\Pr}{Ra}}U_c L \quad , \quad \tau = 3\sqrt{\frac{\Pr}{Ra}}U_c L + \frac{1}{2} \\ \alpha &= \frac{U_c L}{\sqrt{Ra\,\Pr}} \quad , \quad \tau_g = \frac{3U_c L}{2\sqrt{Ra\,\Pr}} + \frac{1}{2} \end{aligned} \tag{27}$$

Note here that in order to avoid significant compressibility errors, the value of U_c should be kept small. Therefore, in the present study we have chosen $U_c = 0.01\,c$ for $Ra = 10^3$ and $U_c = 0.03\,c$ for $Ra = 10^4$, whereas $U_c = 0.1\,c$ for $Ra = 10^5$ and 10^6. Moreover, the working fluid is air with $Pr = 0.7$. The proposed GFTLBM is utilized to treat the surfaces of both of the square cavity and the circular cylinder. A uniform rectangular lattices of sizes 100×100 and 150×150 are used for Rayleigh number 10^3 and 10^4, respectively. For Rayleigh numbers 10^5 and 10^6, however, a 200×200 grid is employed. In order to validate our results, we utilized the results obtained by the CFD software package OpenFOAM (Open Source Field Operation and Manipulation) version 2.1.0 developed by the OpenFOAM Team at SGI Corp. We used a solver based on the finite volume technique say "buoyantBoussinesqSimpleFoam" in which the PCG solver was employed to solve the pressure equation and the "PBiCG" solver was applied to solve the momentum and energy equations. Furthermore, a body-fitted unstructured tetrahedron mesh was employed. For all boundaries, the "fixedValue" boundary condition was used aside from the temperature boundary condition at circular cylinder, which the "zeroGradient" boundary condition was selected. Figure 4, shows a comparison between the associated flow pattern and temperature distribution calculated by GFTLBM and the numerical results taken by OpenFOAM, at several Rayleigh numbers ($Ra = 10^4, 10^5, 10^6$).As expected, the contours are in very good agreement with those obtained by the OpenFOAM software. As can be seen, there is a good agreement between the results of the present method and those computed by the OpenFOAM software. Fig 5 shows the dimensionless local temperature profiles around the circular cylinder for different Rayleigh numbers.

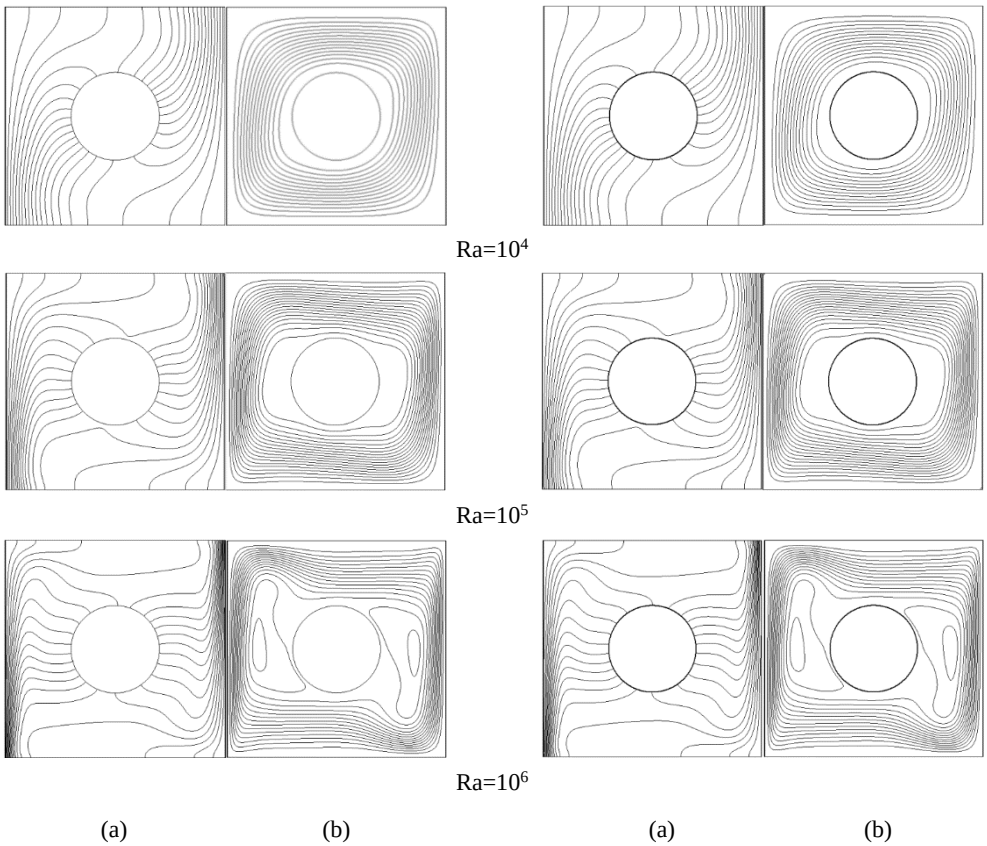

Fig. 4. Comparison of (a) isothermals and (b) streamlines at four different Rayleigh numbers for natural convection phenomenon within a horizontal enclosure with an adiabatic circular cylinder, left: present study; right: the results taken by OpenFOAM.

3.2. Natural Convection in a Concentric Horizontal Annulus with an Outer Isothermal Square Cylinder and an Inner Isoflux Circular Cylinder

As another example to show the ability of the proposed approach, the natural convection of fluid in an annulus at different Rayleigh numbers has been considered. As can be seen from Fig. 3(b), the geometry comprises of a two-dimensional circular cylinder of radius r_c which is located concentrically in rectangular cavity with length L. The cavity walls are maintained at the cold temperature T_C whereas the cylinder wall is kept at a uniform heat flux Q_w. Note here that, both cavity and circular cylinder walls are set to be stationary. The aspect ratio between the square and circular cylinders is

defined as $\lambda = L/2r_c$ and is set to $\lambda = 2.5$. Furthermore, the Boussinesq approximation is followed here again. The dynamic similarity depends on two dimensionless parameters: the Rayleigh number, *Ra*, and the Prandtl number, *Pr*, defined as:

$$Ra = \frac{g\beta\Delta T^* L^3}{\nu\alpha} \quad , \quad Pr = \frac{\upsilon}{\alpha} \tag{28}$$

where, $\Delta T^* = Q_w L/K$, where K is conductivity of fluid. Note here that for all simulations we set $\Delta T^* = 1$. Here**,** the Prandtl number, Pr, was taken to be 0.71, and the Rayleigh number varies over the range $10^3 \le Ra \le 10^6$. In Fig 6, the dimensionless local temperature profiles around the circular cylinder for various Rayleigh numbers are illustrated. As can be seen, there is a good agreement between the results of the present method and those taken by the OpenFOAM. Here, the "fixedGradient" boundary condition was opted for the temperature boundary condition at circular cylinder surface.

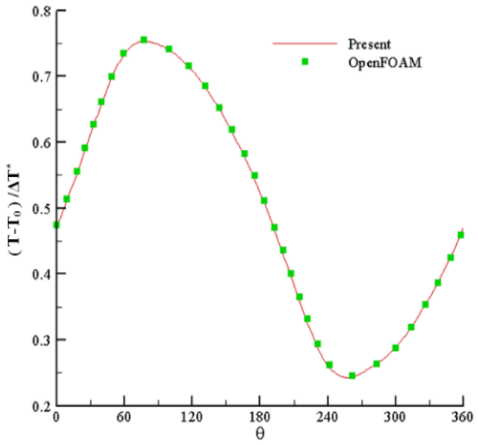

Ra=10^6

Fig. 5. Comparison of local dimensionless temperature around the inner circular cylinder at four different Rayleigh numbers for natural convection phenomenon within a horizontal enclosure with an adiabatic circular cylinder.

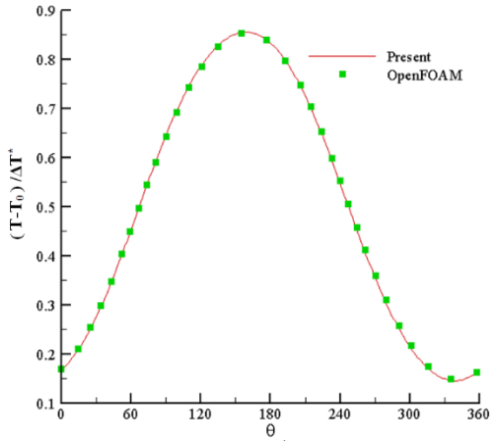

Ra=10^4

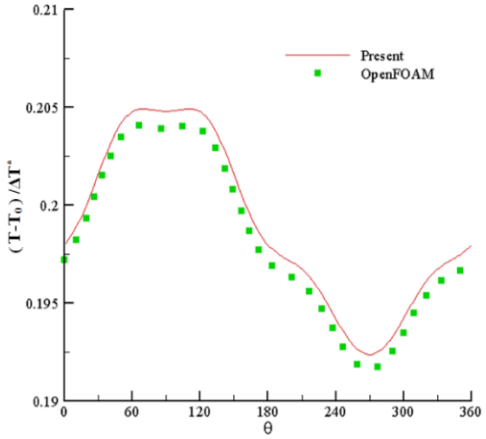

Ra=10^4

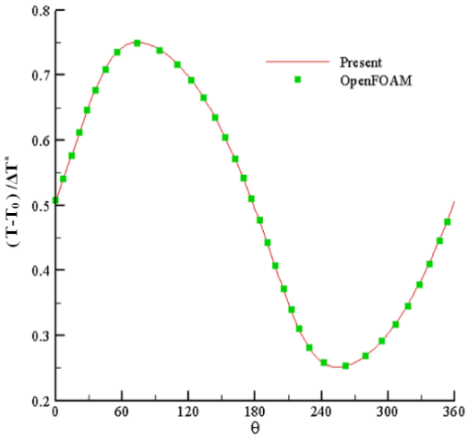

Ra=10^5

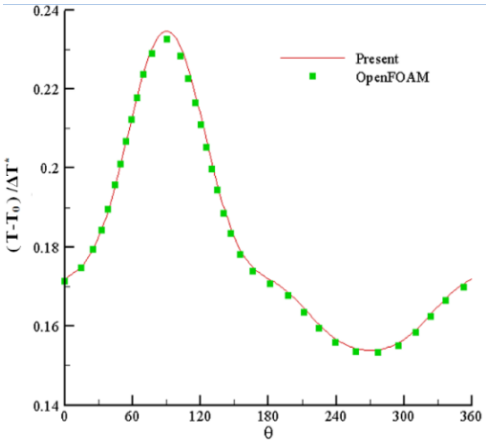

Ra=10^5

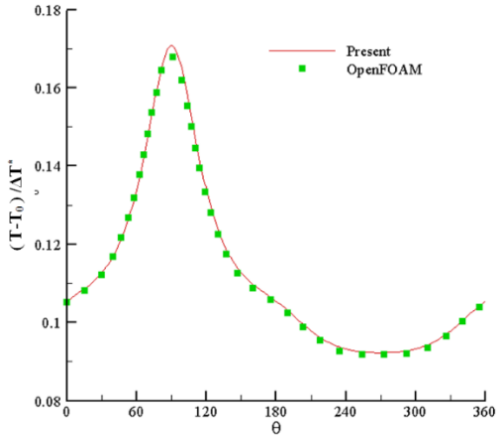

Ra=10^6

Fig. 6. Comparison of local dimensionless temperature around the inner circular cylinder at four different Rayleigh numbers for natural convection phenomenon within an annulus comprised of a circular cylinder in a square enclosure.

In Fig. 7, we compare the associated flow pattern and temperature distribution obtained by GFTLBM and the CFD-based numerical results, at several Rayleigh numbers ($Ra = 10^4$, 10^5,10^6). Inclusively going through the plots, it can be observed that regarding the streamlines, the flow is generally symmetrical about the vertical centerline crossing the middle of the configuration.

Table 1 Comparison of Nu_{avg} for the natural convection in annulus

Ra	Nu_{avg}	
	Present work	OpenFOAM
10^3	5.015	5.039
10^4	5.029	5.048
10^5	5.635	5.663
10^6	9.206	9.253

Due to the buoyancy force, the trapped working fluid undergoes two free circulations. Turning to the isotherms, it is observed that these contours are also perfectly symmetric, regardless of the value of the Rayleigh number. Furthermore, the plots suggest that at low Rayleigh numbers heat transfer is mainly dominated by conduction. As the Rayleigh number approaches higher values, the role of convection in heat transfer becomes more significant. The circulation of the flow grows more and the stagnant area increases at the bottom of the cylinder. Consequently the thermal boundary layer on the surface of the cylinder becomes thinner and a plume forms on the top of the cylinder. At a Rayleigh number as high as 10^6, strong convective flow causes the separation of the boundary layer and as a result, tiny symmetric vortices appear near the bottom wall of the enclosure. As expected, the contours are in very good agreement with those taken by the OpenFOAM software. The Nusselt number is an important parameter, which is used to estimate the rate of heat transfer in thermal phenomenon.

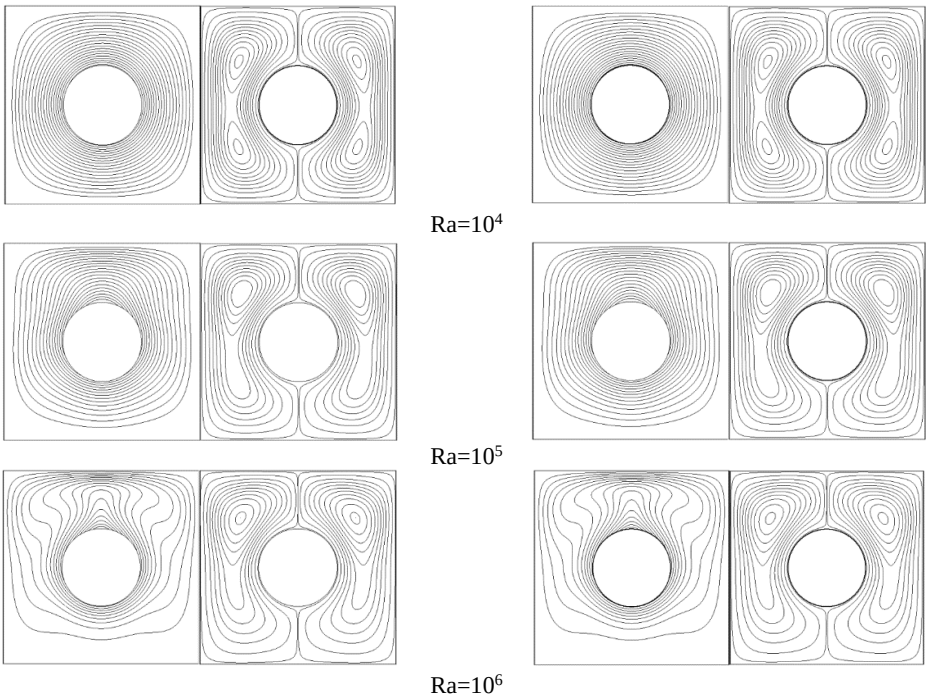

Fig. 7. Comparison of (a) isothermals and (b) streamlines at four different Rayleigh numbers for natural convection phenomenon within an annulus comprised of a circular cylinder in a square enclosure, left: present study; right: the results taken by OpenFOAM.

Here, the average Nusselt number is calculated at the circular cylinder surface via:

$$Nu_{ave} = \frac{\Delta T^*}{2\pi}\int_0^{2\pi}\frac{1}{T(\theta)-T_C}d\theta \qquad (29)$$

A comparison between our results for Nu_{ave}, and those taken by the OpenFOAM software for various Rayleigh numbers has been shown in Table 1. A good agreement is revealed, which shows the accuracy of the present curved boundary treatment. It is also visible that the Rayleigh number has critical contributions in transport characteristics of this phenomenon.

3.3. Natural Convection in a Concentric Horizontal Annulus with an Outer Isothermal Circular Cylinder and an Inner Isoflux Circular Cylinder

In order to further demonstrate ability of the presented thermal boundary condition, another natural convection problem was tested. A schematic of this problem is sketched in Fig. 3 (c).

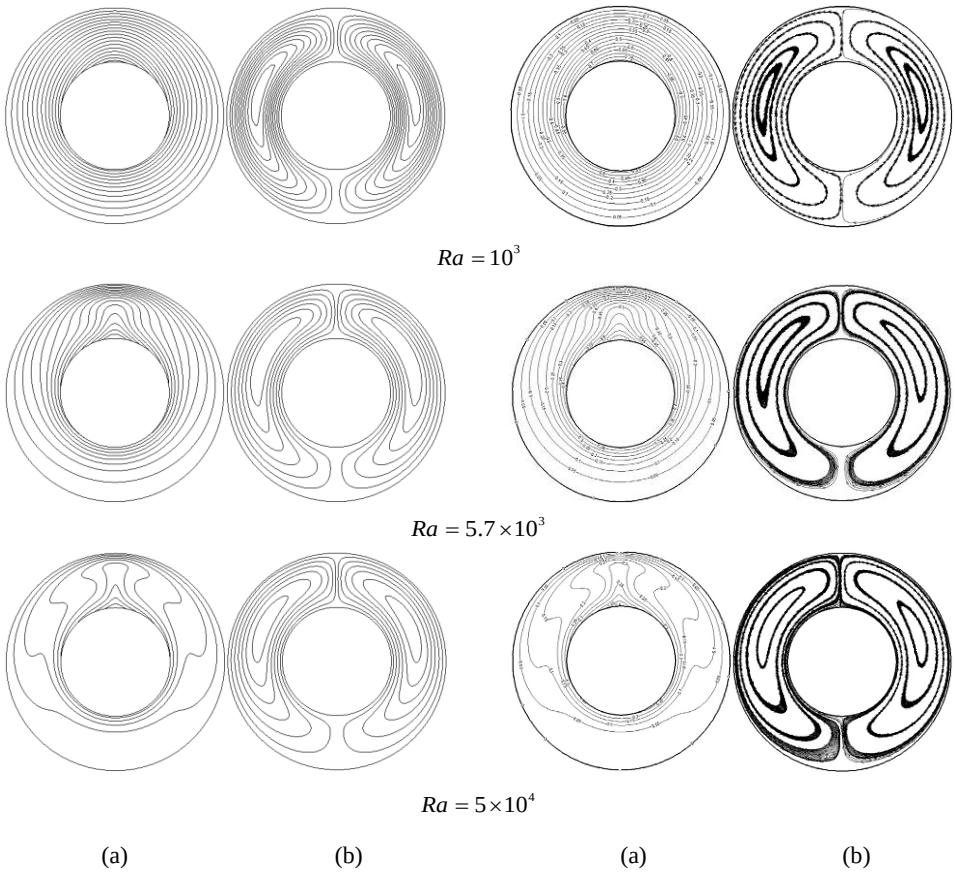

Fig. 8. Comparison of (a) isothermals and (b) streamlines at four different Rayleigh numbers for natural convection phenomenon within a horizontal concentric cylindrical annuli, left: present study; right: Ren *et al*.

As can be seen, the configuration consists of two concentric circular cylinders with inner radius of r_i and outer radius of r_o. The outer cylinder wall is kept at a constant low temperature of T_C, while the inner cylinder wall is maintained at a uniform heat flux Q_w. The aspect ratio between the outer circular cylinder and the inner one is defined as $\lambda = r_o/r_i$ and is set to $\lambda = 2$. Besides, the characteristic length L is defined as the gap between inner and outer cylinder. Moreover, the Boussinesq approximation is adopted here again, and the Rayleigh number varies in the range of $10^3 \le Ra \le 5\times10^4$. Note that, both cylinders do not have any motion. We set $r_i = 30$ for $Ra = 10^3$ and $r_i = 40$ for $Ra = 5.7\times10^3,\ 5\times10^4$. Also a uniform rectangular grid with sizes $2.5r_o$ is used for all cases. Fig. 8 presents the isotherms and streamlines pertained to the case $\lambda = 2$ and for $Pr = 0.7$ and $Ra = 10^3, 5.7\times10^3, 5\times10^4$. The results given by Ren *et al*. (2013) are also included for comparison. They utilized the second-order finite difference scheme to discretize the spatial derivatives. Besides, an implicit direct-forcing IBM was used to handle curved boundary conditions. Considering the streamlines, it is clear that the flow is generally symmetric about the vertical centerline. Due to the buoyancy force, the fluid undergoes two free circulations. From the plots, it is found that according to the isotherms, these contours are also completely symmetrical, regardless of the value of

the Rayleigh number. A detailed physical interpretation of the flow and heat transfer phenomena related to this case study has been discussed by J.S. Yoo (2003).

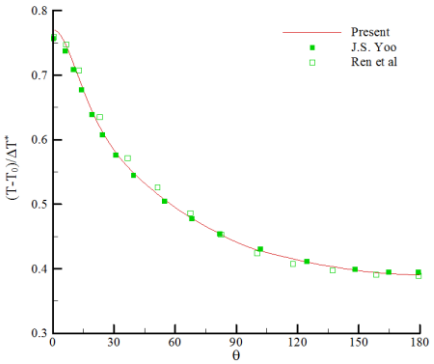

Ra=5700

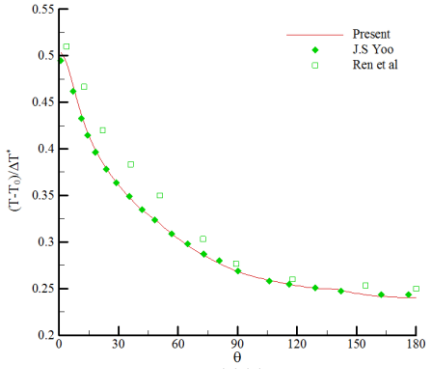

Ra=50000

Fig. 9. Comparison of local dimensionless temperature around the inner circular cylinder at four different Rayleigh numbers for natural convection phenomenon within concentric cylindrical annuli

As can be observed, the contours are in very good agreement with those from Ren *et al*. (2013). Comparison between our results and the numerical data taken from Ren *et al*. (2013) and J.S. Yoo (2003) for dimensionless local temperature distribution around the inner circular cylinder are presented in Fig. 9 for $Ra = 10^3,\ 5.7\times10^3,\ 5\times10^4$.

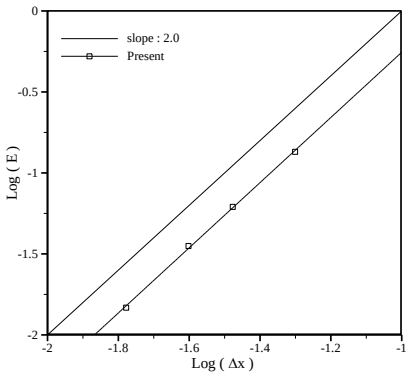

Fig. 10. Relative L_2 norm for the Nusselt number versus the lattice spacing Δx in a log–log scale.

One may confirm that in terms of accuracy, the achievements of this study exhibit good agreement with those of J.S. Yoo (2003) (They applied the vorticity-stream function method and a finite difference scheme to solve momentum and energy equations respectively). Fig. 10 presents the relative global L_2 norm error in Nusselt number in logarithmic scales against the grid spacing Δx. The study has been performed for $Ra = 10^5$ It is revealed that the overall numerical method is second order accurate in space.

3.4. Natural Convection in an Eccentric Horizontal Annulus with an Outer Isothermal Circular Cylinder and an Inner Isoflux Circular Cylinder

Natural convection in a horizontal eccentric annulus at different values of the Rayleigh numbers is tested here to validate the applicability of the presented method more. A schematic of this problem has been illustrated in Fig. 3 (d). As can be seen, the configuration consists of two eccentric circular cylinders with inner radius of r_i and outer radius of r_o. The outer cylinder wall is set to a constant low temperature of T_C, while a uniform heat flux Q_w is imposed on the inner cylinder wall. The aspect ratio between the outer and inner circular cylinders is evaluated as $\lambda = r_o/r_i$ and is set to $\lambda = 2.6$. The gap between the inner and the outer cylinders is considered as the characteristic length L. Moreover, eccentricity is defined as $\varepsilon = \delta/L$, where, δ is the distance between the centers of two cylinders. The Boussinesq approximation is adopted here again, and the Rayleigh number varies in the range $10^3 \le Ra \le 10^6$. Both cylinders are maintained at rest. We set $r_i = 30$ for $Ra = 10^3,\ 10^4$ and $r_i = 40$ for $Ra = 10^5,\ 10^6$.

Table 2 Comparison of Nu_{avg} for the natural convection in eccentric annulus

Ra	Nu_{avg}			
	Present work	Ho *et al*.	Ren *et al*.	OpenFOAM
10^3	2.2945	2.2724	2.3418	2.3155
10^4	3.1500	3.2071	3.2052	3.1698
10^5	4.5139	4.4821	4.5309	4.5283
10^6	7.0034	6.8942	6.8879	6. 9834

Figure. 11 presents the isotherms and streamlines pertained to the case $\varepsilon = -0.625$, for $Pr = 0.7$ and $Ra = 10^4,\ 10^5$ and 10^6. The results obtained by the OpenFOAM software are also included for comparison. As can be observed, the contours are in very good agreement with those from the OpenFOAM software.

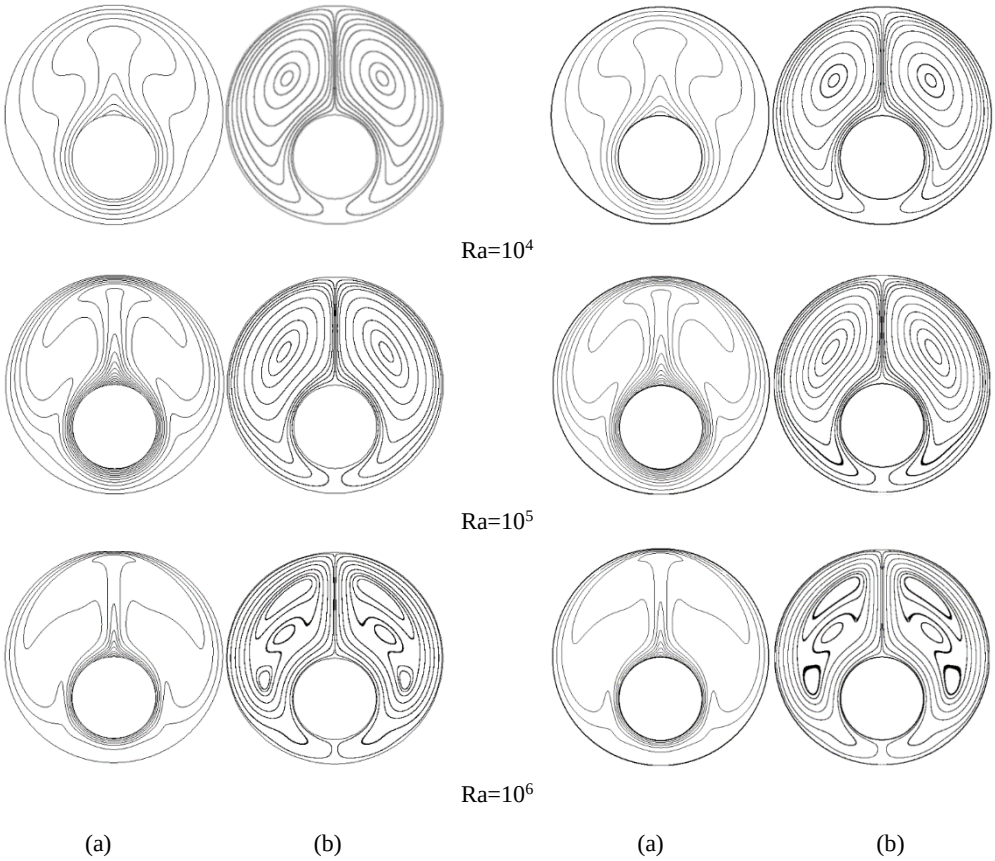

Fig. 11. Comparison of (a) isothermals and (b) streamlines at four different Rayleigh numbers for natural convection phenomenon within an eccentric cylindrical annulus, left: present study; right: the results taken by OpenFOAM.

In Table 2, the average Nusselt number at various values of the Rayleigh number are presented to compare with numerical results published by Ren *et al*. (2013) and Ho *et al*. (1989), and the result achieved by the Open FOAM software. As expected, the values are in very good agreement with those from **(**Ren, Shu and Yang 2013; Ho, Lin and Chen 1989**),** and those obtained by OpenFOAM software.

4. CONCLUSION

A thermal ghost fluid lattice Boltzmann method (Khazaeli, Mortazavi and Ashrafizaadeh 2013) was improved to properly simulate thermal flows within complex geometries with heat flux boundary conditions. The present approach is general, relatively simple and is globally second order accurate. It also benefits from using a Cartesian grid. In this method, boundary conditions are imposed by applying a ghost fluid method. Both natural and forced convection problems were simulated to verify the ability of the present approach. It was observed that our results are in a good agreement with those of other numerical efforts. It is concluded that the present treatment can be used with confidence to simulate problems containing complex geometries with heat flux boundary conditions.

REFERENCES

Alexander, F. J., S. Chen, and J. D. Sterling (1993). Lattice Boltzmann *thermohydrodynamics. Physical Review E*, 47(4), 2249-2259.

Bartoloni, A., C. Battista, and S. Cabasino (1993). LBE simulation of Rayleigh–Bénard convection on the APE100 parallel processor. *Internatinal Journal of Modern Physics C*, 4(5), 993-1006.

Chang, C., C. H. Liu, and C. A. Lin (2009). Boundary conditions for lattice Boltzmann simulations with complex geometry flows, *Comput Math Appl*, 58:940.

Chaudhuri, A., A. Hadjadj, and A. Chinnayya (2011). On the use of immersed boundary methods for shock/obstacle interactions, *J. Comput. Phys*. 230, 1731-1748.

Chen, Y., H. Ohashi, and M. Akiyama, (1994). Thermal lattice Bhatnagar–Gross–Krook model without nonlinear deviations in macrodynamic equations. *Physical Review E*, 50(6), 2776-2783.

Chen, S., D. Martínez, and R. Mei (1996). On boundary conditions in lattice Boltzmann methods. *Physics of Fluids*, 8(9), 2527-2536.

Chen, S. and G. D. Doolen (1998). Lattice Boltzmann method for fluid flow. *Annual Review of Fluid Mechanics*, 30, 329-364.

Cornubert, R., D. d'Humières, and D. Levermore (1991). A Knudsen layer theory for lattice gases, *Physica* D, 47(1-2), 241-247.

D'Orazio, A., M. Corcione, and G.P. Celata (2004). Application to natural convection enclosed flows of a lattice Boltzmann BGK model coupled with a general purpose thermal boundary condition. *International Journal Thermal Science*, 43(6), 575-586.

Fedkiw, R. P., T. Aslam, B. Merriman, and S. Osher (1999). A non-oscillatory Eulerian approach to interfaces in multimaterial flows (the Ghost Fluid Method), *J. Comput. Phys*. 152, 457–492.

Feng, Z. and E. Michaelides (2004). The immersed boundary-lattice Boltzmann method for solving fluid-particles interaction problems. *Journal of Computational Physics*, 195(2), 602–628.

Filippova, O. and Hänel, D. (1998). Boundary fitting and local grid refinement for lattice BGK models, *Int. J. Mod. Phys*. C 9 1271–1279.

Guo, Z. L., C. G. Zheng, and B. C. Shi (2002). An extrapolation method for boundary conditions in lattice Boltzmann method, *Phys. Fluids* 14 (6) 2007–2010.

He, X., S. Chen, and G. D. Doolen (1998). A novel thermal model for the lattice Boltzmann method in incompressible limit. *Journal of Computational Physics*, 146(1), 282-300.

Ho, C. J., Y. H. Lin, and T. C. Chen (1989). A numerical study of natural convection in concentric and eccentric horizontal cylindrical annuli with mixed boundary conditions, *Int. J. Heat Fluid Flow* 10, 40–47.

Huang, H., T. S. Lee, and C. Shu (2006). Thermal curved boundary treatment for the thermal lattice boltzmann equation, *Int. J. Mod. Phys. C*. 17 (5), 631-643.

Jeong, H. K., H. S. Yoon, M. Y. Ha, and M. Tsutahara (2010). An immersed boundary-thermal lattice Boltzmann method using an equilibrium internal energy density approach for the simulation of flows with heat transfer. *Journal of Computational Physics*, 229(7), 2526-2543.

Kang, S. K. and Y. A. Hassan (2010). A comparative study of direct-forcing immersed boundary-Lattice Boltzmann methods for stationary complex boundaries. International *Journal for Numerical Methods in Fluids*, 66(9), 1132-1158.

Kang, S. K. and Y. A. Hassan (2011). A direct-forcing immersed boundary method for the thermal lattice Boltzmann method. *Computers & Fluids*, 49(1), 36-45.

Kao, P. -H. and R. -J. Yang (2008). An investigation into curved and moving boundary treatments in the lattice Boltzmann method. *Journal of Computational Physics*, 227(11), 5671-5690.

Khazaeli, R., S. Mortazavi, and M. Ashrafizaadeh (2013). Application of a ghost fluid approach for a thermal lattice Boltzmann method. *Journal of Computational Physics*, 250(Oct.), 126–140.

Li, L., R. Mei and J. F. Klausner (2013). Boundary conditions for thermal lattice Boltzmann equation method, *J. Comput. Phys*. 237, 366–395.

Li, Q., Y. L. He, Y. Wang, and G. H. Tang (2008). An improved thermal lattice Boltzmann model for flows without viscous heat dissipation and compression work, *International Journal of Modern Physics* C, 19(01), 125-150.

Lin, K. H., C. C. Liao, S.Y. Lien, and C. A. Lin (2012). Thermal lattice Boltzmann simulations of natural convection with complex geometry, *J. Comp. Fluids* 69, 35–44.

Liu, C. H., K. H. Lin, H. C. Mai, and C. A. Lin (2010). Thermal boundary conditions for thermal lattice Boltzmann simulations, *Computers & Mathematics with Applications* 59(7), 2178-2193.

Mei, R., L. S. Luo, and W. Shyy (1999). An accurate curved boundary treatment in the lattice Boltzmann method, *J. Comput. Phys*. 155, 307–330.

Mittal, R., H. Dong, M. Bozkurttas, and F. M. Najjar (2008). A versatile sharp interface immersed boundary method for incompressible flows with complex boundaries, *J. Comput. Phys*. 227 (10), 4825–4852.

McNamara, G. and B. Alder (1993). Analysis of the lattice Boltzmann treatment of hydrodynamics. Physica A*: Statistical Mechanics and its Applications*, 194(1-4), 218- 228.

Niu, X.D., C. Shu, Y.T. Chew and Y. Peng (2006). A momentum exchange-based immersed boundary-lattice Boltzmann method for simulating incompressible viscous flows. *Physics Letters A*, 354(3), 173-182.

Noble, D.R., S. Chen, J.G. Georgiadis and R.O. Buckius (1995). A consistent hydrodynamic boundary condition for the lattice Boltzmann method. *Physics of Fluids*, 7(1), 203-209.

Pan, D. (2010). A simple and accurate ghost cell method for the computation of incompressible flows over immersed bodies with heat transfer, *Numer. Heat Transfer* B. 58, 17–39.

Peng, Y., C. Shu and Y.T. Chew (2003). Simplified thermal lattice Boltzmann model for incompressible thermal flows, *Physical Review* E, 68(026701), 1-8.

Peng, Y., C.Shu, Y.T. Chew, X.D. Niu and X.Y. Lu (2006). Application of multi-block approach in the immersed boundary-lattice Boltzmann method for viscous fluid flows. *Journal of Computational Physics*, 218(2), 460-478.

Peskin, C.S. (1972). Flow patterns around heart valves: a numerical method. *Journal of Computational Physics*, 10(2), 252-271.

Qian, Y.H., D. d. 'Humières and P. Lallemand (1992). Lattice BGK model for Navier-Stokes equation. Europhysics Letters, 17(6), 479.

Ren, W., C. Shu and W. Yang (2013). An efficient immersed boundary method for thermal flow problems with heat flux boundary conditions, Int. *J. Heat Mass Transfer* 46, 694–705.

Shan, X. (1997). Simulation of Rayleigh–Bénard convection using a lattice Boltzmann method, *Physical Review* E, 55(3), 2780-2787.

Shi, Y., T.S. Zhao and Z.L. Guo (2004). Thermal lattice Bhatnagar-Gross-Krook model for flows with viscous heat dissipation in the incompressible limit. Physical Review E, 70(1), 066310.

Tang, G.H., W.Q. Tao and Y.L. He (2005). Thermal boundary condition for the thermal lattice Boltzmann equation. *Physical Review E*, 72(01), 016703.

Tiwari, A. and Vanka, S.P. (2012). A ghost fluid Lattice Boltzmann method for complex geometries, *Int. J. Numer. Meth. Fluids* 69, 481-498.

Verschaeve, J.C.G. (2010). A curved no-slip boundary condition for the lattice Boltzmann method, *J. Comp. Phys*. 229, 6781–6803.

Wu, J. and C. Shu (2009). Implicit velocity correction-based immersed boundary-lattice Boltzmann method and its applications. *Journal of Computational Physics*, 228(6), 1963-1979.

Yin, X. and Zhang, J. (2012). An improved bounce-back scheme for complex boundary conditions in lattice Boltzmann method, *J. Comput. Phys*. 231, 4295–4303.

Yoo, J.S. (2003). Dual free-convective flows in a horizontal annulus with a constant heat flux wall, *Int. J. Heat Mass Transfer* 46, 2499–2503.

Ziegler, D.P. (1993). Boundary conditions for lattice Boltzmann simulations. *Journal of Statical Physics*, 71(5-6), 1171-1177.

Zou, Q. and X. He (1997). On pressure and velocity boundary conditions for the lattice Boltzmann BGK model. *Physics of Fluids*, 9(6), 1591-1598.